

Article

Decoupling Control for Module Suspension System of Maglev Train Based on Feedback Linearization and Extended State Observer

Qicai Li , Peng Leng *, Peichang Yu, Danfeng Zhou, Jie Li and Minghe Qu

College of Intelligence Science and Technology, National University of Defense Technology, Changsha 410073, China; lqc717@nudt.edu.cn (Q.L.); yupeichang@nudt.edu.cn (P.Y.); zhoudanfeng@nudt.edu.cn (D.Z.); jieli@nudt.edu.cn (J.L.); quminghe@nudt.edu.cn (M.Q.)

* Correspondence: lengpeng17@nudt.edu.cn

Abstract: The suspension gap of the electromagnetic suspension maglev train is around 8 mm. In practice, it is found that the system gap fluctuations are amplified due to the inner coupling of the suspension module system in the maglev train. In addition, maglev trains are affected by load disturbances and parameter perturbations during operation. These uncertainties reduce the ride comfort. Therefore, it is necessary to propose a novel control strategy to suppress inner coupling while reducing the influence of uncertainties on the system. In this paper, a control strategy based on feedback linearization and extended state observer (ESO) is proposed to address this challenge. Firstly, the suspension module system model is established with parameter uncertainties and external disturbances. Additionally, the inner coupling of the suspension module is represented in this model. Subsequently, the feedback linearization method based on differential geometry theory is applied to reduce the effect of inner coupling. Meanwhile, the system uncertainties are transformed into equivalent disturbances by this method. Afterward, a linear ESO is designed to estimate the equivalent disturbances. Finally, a state feedback controller is used to achieve stable suspension and compensate for the disturbances. Simulation and experimental results show that the proposed decoupled control strategy significantly suppresses the influence of inner coupling and uncertainties on the system compared with the traditional PID control strategy.

Keywords: maglev train; suspension module control; feedback linearization; decoupling control; extended state observer



Citation: Li, Q.; Leng, P.; Yu, P.; Zhou, D.; Li, J.; Qu, M. Decoupling Control for Module Suspension System of Maglev Train Based on Feedback Linearization and Extended State Observer. *Actuators* **2023**, *12*, 342. <https://doi.org/10.3390/act12090342>

Academic Editors: Jun Zheng and Mochimitsu Komori

Received: 25 July 2023

Revised: 19 August 2023

Accepted: 24 August 2023

Published: 25 August 2023



Copyright: © 2023 by the authors. Licensee MDPI, Basel, Switzerland. This article is an open access article distributed under the terms and conditions of the Creative Commons Attribution (CC BY) license (<https://creativecommons.org/licenses/by/4.0/>).

1. Introduction

Maglev trains has gradually attracted extensive attention for advantages, which include low noise, low energy consumption, high climbing capacity, and environmental friendliness [1,2]. Over the past 50 years, maglev train technology has undergone significant development and has been commercially implemented in several countries. Noteworthy examples include the Transrapid in Germany, High Speed Surface Transport (HSST) in Japan, Urban Transit Maglev (UTM) in Korea, and Beijing S1 line in China [3–7].

Figure 1a shows the lateral view of an electromagnetic suspension (EMS) maglev train. The EMS maglev train maintains the suspension gap at 7–10 mm, relying on the electromagnetic attraction generated by the suspension module. In recent years, many studies have been conducted to improve the system performance [8–10]. However, most of them center around single-suspension-point models and neglect the holistic nature of the suspension module. Figure 1b shows the structure of a suspension module. A suspension module consists of two sets of electromagnets, two sets of sensors, and brackets. The electromagnets are rigidly connected by brackets, and each set of electromagnet coils is connected in series to form a suspension point. The track of the maglev train is segmented. Each section of the track is connected by a track joint. Due to factors such as foundation

settlement, temperature changes, and track installation errors, there may be a height difference at the track joint, which is called track step [11]. The suspension points undergo significant fluctuation while passing through the track steps.

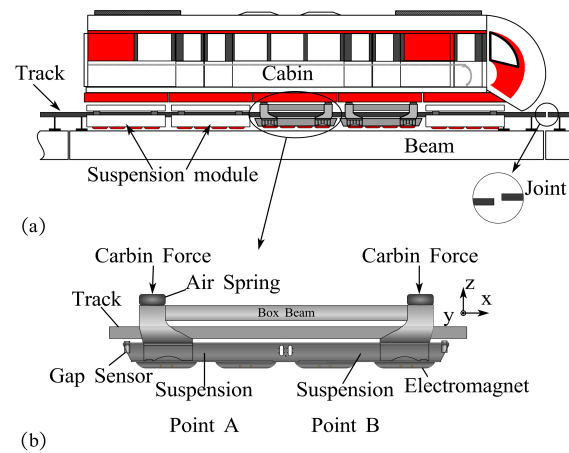


Figure 1. Lateral view of the medium-low-speed maglev train. (a) A maglev train running on the track; (b) structure of the suspension module.

Figure 2 shows the effect of track steps on the suspension module. It can be observed that fluctuations in one suspension point affect the suspension gap of another suspension point. If the difference of the track steps is too high, the suspended module may vibrate or even hit the track, which will reduce the safety of the train. Scholars have applied active suspension systems to magnetic levitation systems to reduce the influence of track irregularities on ride comfort [12,13]. On the other hand, several scholars have tackled this challenge by designing appropriate suspension control algorithms.

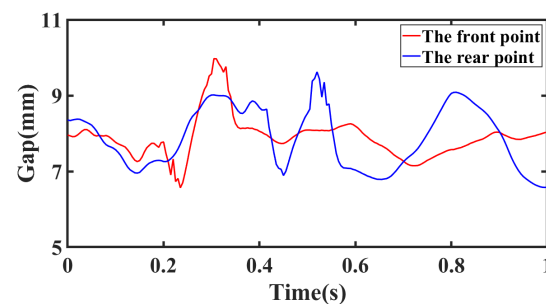


Figure 2. The gap curves of the suspension module through the track joint.

The suspension control system for the suspension module is a two-input and two-output (TITO) system [14]. Various methods have been explored for decoupling multiple-input multiple-output (MIMO) systems, including inverse Nyquist array [15], differential geometric approach [16], sliding mode control [17], and neural networks [18]. Some of these methods have been applied to decouple the suspension module system. Liu et al. [19] proposed a decoupling control algorithm based on feedback linearization to decouple the suspension module system and achieve the desired performance of decoupling and suspension. Afterwards, some scholars conducted further research based on this study. Leng et al. [20] proposed a new equivalent gap calculation method based on the geometrical relationship between the suspension module and the track when passing through the joints and verified the performance of the method in experiments. He et al. [21] proposed a decoupling controller based on linear quadratic regulator (LQR) theory and designed disturbance nonlinear observers to improve the system robustness. The experimental results illustrate that the method has the desired decoupling performance. However, the control performance of the system when perturbed is not experimentally verified. In

addition, decoupling can also be achieved by treating the coupling effects of the suspension module as perturbations and compensating for them. Sun et al. [22] proposed a control method that combines a backstepping controller and an ESO. The external perturbations at the suspension point are estimated by the ESO and compensated in the backstepping controller. Numerical simulations have demonstrated the effectiveness of this method.

To further improve the performance of the maglev train, it is crucial to consider the impact of load variations and parameter perturbations in the system. When the train operates on curved tracks, the balance between the centrifugal force and electromagnetic force must be maintained. On the other hand, the increase or decrease in passengers directly affects the load of the train. Excessive variations in external loads may degrade control performance, and even affect driving safety of the train. In addition, there are un-modeled dynamics and parameter perturbations in the suspension system so that it is difficult to model precisely [23]. In order to tackle these challenges, several research studies have been conducted. Chen et al. [24] constructed a T-S fuzzy model that considered parameter uncertainties and external disturbances. The fuzzy adaptive control method was used to perform suspension control. In addition, a particle swarm optimization (PSO) algorithm is applied to further suppress the effect of parameter uncertainties. Sun et al. [25] designed a robust control law based on the nonlinear model. This method avoids approximation errors caused by linearization. A modified backstepping sliding mode controller is proposed to suppress the effect of disturbances on the system. Ni et al. [26] constructed a disturbance observer-based controller based on an improved nonlinear mathematical model of electromagnetic force. The effectiveness of the proposed method has been tested by simulations and experiments. Refs. [27,28] proposed disturbance observer-based control methods to effectively increase the system stability. Sun et al. [29] proposed an adaptive robust controller. The influence of time delays and disturbances on the system is effectively suppressed. In addition, several scholars have applied artificial intelligence algorithms to tackle the challenge, such as neural networks [30–32], optimization techniques [33,34], genetic algorithms [35], and so on.

In this paper, the suspension module system model considering both parameter uncertainties and external disturbances is constructed. A state feedback decoupling controller based on feedback linearization is used to reduce the effect of inner coupling between suspension points. Furthermore, to eliminate the dependence of the feedback linearization control method on the exact parameters of the system and enhance system robustness, the model errors and external uncertainties are equivalent to the external inputs of the subsystems. Then, a mature state feedback controller is designed to achieve stable suspension. Afterward, an ESO is employed to estimate the equivalent uncertainties of the system. Finally, the equivalent uncertainties are compensated in the controller based on the ESO observations. Simulations and experimental results demonstrate that the proposed strategy can effectively suppress the effect of inner coupling and uncertainties on the system.

The rest of the paper is organized as follows. Section 2 provides the mathematical modeling process of the suspension module system. Section 3 presents the decoupling control strategy based on ESO. Section 4 shows the results and analysis of the simulations and experiments. Section 5 gives the conclusions of this paper.

2. Modeling of the Module Suspension System

To construct the mathematical model of the suspension module, certain assumptions are made about the structure diagram shown in Figure 1, as follows:

1. Magnetic flux leakage of the winding and the magnetoresistance of the iron core and guide are ignored.
2. There is no misalignment between the pole surface and the orbit of the electromagnet.
3. The mass distribution of the suspension module is uniform.

According to the above assumptions, the force diagram of the suspension module is shown in Figure 3.

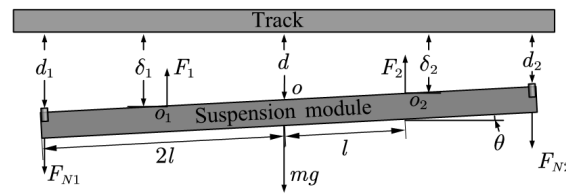


Figure 3. The force diagram of the suspension module.

F_1 and F_2 are the electromagnetic forces on the two suspension points; δ_1 and δ_2 are the gaps between the two suspension points and the track; d_1 and d_2 are the gaps measured by the sensors; d is the gap between the center of the suspension module and the track; l is the length of an electromagnet; F_{N1} and F_{N2} are the forces of air springs acting on both sides of the suspension module; mg is the gravity of the suspension module.

The pitch angle θ is less than 0.5° during normal operation. It can be assumed that $\theta \approx \sin \theta \approx \tan \theta$. According to the geometric relationship, the following equation is satisfied between d_1, d_2 and $\delta_1, \delta_2, \theta$:

$$\begin{cases} \delta_1 = \frac{3d_1 + d_2}{4} \\ \delta_2 = \frac{d_1 + 3d_2}{4} \\ \theta = \frac{d_1 - d_2}{4l} \end{cases} \quad (1)$$

The motion of the suspension module consists of translational motion along the center of mass and rotation around the center of mass. Forces in the downward direction and counterclockwise direction are defined as positive. According to Newton’s law, the dynamic equations of the suspension system are as follows:

$$\begin{cases} m\ddot{d} = mg - F_1 - F_2 + F_{N1} + F_{N2} + \Delta F_{N1} + \Delta F_{N2} \\ J\ddot{\theta} = -F_1 \cos \theta \cdot l + 2F_{N1} \cos \theta \cdot l + F_2 \cos \theta \cdot l - 2F_{N2} \cos \theta \cdot l \end{cases} \quad (2)$$

where ΔF_{N1} and ΔF_{N2} are load disturbances of two suspension points; J is the rotational inertia of the suspension module around the center of mass. Equation (2) can be approximated as Equation (3) since $\cos \theta \approx 1$.

$$\begin{cases} m\ddot{d} = mg - F_1 - F_2 + F_{N1} + F_{N2} + \Delta F_{N1} + \Delta F_{N2} \\ J\ddot{\theta} = -F_1 \cdot l + 2F_{N1} \cdot l + F_2 \cdot l - 2F_{N2} \cdot l + \Delta F_e \end{cases} \quad (3)$$

where ΔF_e is the approximation error.

The formula for calculating the electromagnetic force is as follows:

$$F_j = \frac{\mu_0 N^2 A}{4} \frac{i_j^2}{\delta_j^2} + \Delta F_j = K \frac{i_j^2}{\delta_j^2} + \Delta F_j, j = 1, 2 \quad (4)$$

where i_1, i_2 are the coil current of the two suspension points; N is number of coil turns of each electromagnet; A is the effective area of each magnet pole; g is the acceleration of gravity; μ_0 is the permeability of a vacuum; and $\Delta F_1, \Delta F_2$ denote the model error.

The relationship between the current i and the voltage u of the electromagnets is as follows:

$$i_j = \frac{\delta_j}{2K} (u_j - Ri_j) + \frac{i_j}{\delta_j} \delta_j + u_{pj}, j = 1, 2 \quad (5)$$

where u_{p1}, u_{p2} denote the perturbations in the current loop; R is the resistance of a set of electromagnets.

In summary, selecting $X = [x_1, x_2, x_3, x_4, x_5, x_6]^T = [d_1, \dot{d}_1, i_1, d_2, \dot{d}_2, i_2]^T$ as the state vector, the state-space equations of the suspension module can be obtained as follows:

$$\begin{cases} \dot{x}_1 = x_2 \\ \dot{x}_2 = -\frac{40}{m} \frac{Kx_3^2}{(3x_1+x_4)^2} + \frac{8}{m} \frac{Kx_6^2}{(x_1+3x_4)^2} + \frac{2}{m}(2F_{N_1} - F_{N_2}) + g + f_{p1} \\ \dot{x}_3 = \frac{3x_1+x_4}{8K} u_1 - R \frac{3x_1+x_4}{8K} x_3 + \frac{3x_2+x_5}{3x_1+x_4} x_3 + u_{p1} \\ \dot{x}_4 = x_5 \\ \dot{x}_5 = \frac{8}{m} \frac{Kx_3^2}{(3x_1+x_4)^2} - \frac{40}{m} \frac{Kx_6^2}{(x_1+3x_4)^2} + \frac{2}{m}(2F_{N_2} - F_{N_1}) + g + f_{p2} \\ \dot{x}_6 = \frac{x_1+3x_4}{8K} u_2 - R \frac{x_1+3x_4}{8K} x_6 + \frac{x_2+3x_5}{x_1+3x_4} x_6 + u_{p2} \end{cases} \tag{6}$$

where f_{p1} and f_{p2} are the uncertainties, which are as follows:

$$\begin{cases} f_{p1} = -\frac{5}{2m} \Delta F_1 + \frac{1}{2m} \Delta F_2 + \frac{4}{m} \Delta F_{N1} - \frac{2}{m} \Delta F_{N2} + \frac{1}{6ml} \Delta F_e \\ f_{p2} = \frac{1}{2m} \Delta F_1 - \frac{5}{2m} \Delta F_2 - \frac{2}{m} \Delta F_{N1} + \frac{4}{m} \Delta F_{N2} - \frac{1}{6ml} \Delta F_e \end{cases}$$

3. Decoupling Controller Design

3.1. Feedback Decoupling

According to Equation (6), the standard state-space equation of the suspension module is as follows:

$$\begin{cases} \dot{x} = f(x) + g(x)u + p \\ y = h(x) \end{cases} \tag{7}$$

where x is the state vector; u is the input vector; p is the uncertainties of the system; y is the output vector; f , g , and h are the functions about state vector x . The expressions are as follows:

$$f(x) = \begin{bmatrix} x_2 \\ -\frac{40Kx_3^2}{m(3x_1+x_4)^2} + \frac{8Kx_6^2}{m(x_1+3x_4)^2} + \frac{2}{m}(2F_{N_1} - F_{N_2}) + g \\ -R \frac{3x_1+x_4}{8K} x_3 + \frac{3x_2+x_5}{3x_1+x_4} x_3 \\ x_5 \\ \frac{8Kx_3^2}{m(3x_1+x_4)^2} - \frac{40Kx_6^2}{m(x_1+3x_4)^2} + \frac{2}{m}(2F_{N_2} - F_{N_1}) + g \\ -R \frac{x_1+3x_4}{8K} x_6 + \frac{x_2+3x_5}{x_1+3x_4} x_6 \end{bmatrix}$$

$$g(x) = \begin{bmatrix} 0 & 0 \\ 0 & 0 \\ \frac{3x_1+x_4}{8K} & 0 \\ 0 & 0 \\ 0 & 0 \\ 0 & \frac{x_1+3x_4}{8K} \end{bmatrix}, p = \begin{bmatrix} 0 \\ f_{p1} \\ u_{p1} \\ 0 \\ f_{p2} \\ u_{p2} \end{bmatrix}$$

$$u = \begin{bmatrix} u_1 \\ u_2 \end{bmatrix}, h(x) = \begin{bmatrix} h_1(x) \\ h_2(x) \end{bmatrix} = \begin{bmatrix} x_1 \\ x_4 \end{bmatrix}$$

According to the differential geometry theory, it can be calculated as follows:

$$\begin{aligned}
 L_f^0 h(x) &= \begin{bmatrix} x_1 \\ x_4 \end{bmatrix}, L_f^1 h(x) = \begin{bmatrix} x_2 \\ x_5 \end{bmatrix}, L_f^2 h(x) = \begin{bmatrix} f_2(x) \\ f_5(x) \end{bmatrix}, \\
 L_g L_f^0 h(x) &= L_g L_f^1 h(x) = 0, L_p L_f^0 h(x) = 0, \\
 L_p L_f^1 h(x) &= \begin{bmatrix} f_{p1} \\ f_{p2} \end{bmatrix}, d(L_p L_f^1 h(x)) / dt = \begin{bmatrix} \dot{f}_{p1} \\ \dot{f}_{p2} \end{bmatrix}, \\
 L_f^3 h(x) &= \begin{bmatrix} \frac{10Rx_3^2}{m(3x_1+x_4)^2} - \frac{2Rx_6^2}{m(x_1+3x_4)^2} \\ -\frac{2Rx_3^2}{m(3x_1+x_4)^2} + \frac{10Rx_6^2}{m(x_1+3x_4)^2} \end{bmatrix}, \\
 L_g L_f^2 h(x) &= \begin{bmatrix} -\frac{10x_3}{m(3x_1+x_4)} & \frac{2x_3}{m(3x_1+x_4)} \\ \frac{2x_6}{m(x_1+3x_4)} & -\frac{10x_6}{m(x_1+3x_4)} \end{bmatrix}, \\
 L_p L_f^2 h(x) &= \begin{bmatrix} -\frac{80Kx_3u_{p1}}{m(3x_1+x_4)^2} + \frac{16Kx_6u_{p2}}{m(x_1+3x_4)^2} \\ \frac{16Kx_3u_{p1}}{m(3x_1+x_4)^2} - \frac{80Kx_6u_{p2}}{m(x_1+3x_4)^2} \end{bmatrix}.
 \end{aligned}$$

where $L_f^0 h(x)$ is denoted as the Lie derivative of the function $h(x)$ along the vector field $f(x)$.

The following equation can be derived from the above calculation results:

$$\begin{aligned}
 L_g L_f^0 h(x) &= 0 \\
 L_g L_f^1 h(x) &= 0, (j = 1, 2) \\
 L_g L_f^2 h(x) &\neq 0
 \end{aligned} \tag{8}$$

According to the discriminant condition of relative order, the relative order vector of the module suspension system is $[r_1(x_0) \ r_2(x_0)] = [3 \ 3]$, which satisfies $r_1(x_0) + r_2(x_0) = 6$. Therefore, the model of the suspension system satisfies the linearization condition.

Defining $d^3y/dt^3 = v$, we can obtain the following:

$$\begin{cases} v = v_0 + v_p \\ v_0 = L_f^3 h(x) + L_g L_f^2 h(x) \cdot u \\ v_p = L_p L_f^2 h(x) + d(L_p L_f^2 h(x)) / dt \end{cases} \tag{9}$$

where v_0 is output of the controller; v_p denotes the equivalent uncertainty.

Therefore, the feedback control law of the suspension module is as follows:

$$\begin{aligned}
 u &= \left(L_g L_f^2 h(x) \right)^{-1} \left(v_0 - L_f^3 h(x) \right) \\
 &= \begin{bmatrix} Rx_3 - m \frac{5v_{10} + v_{20}}{48} \frac{3x_1 + x_4}{x_3} \\ Rx_6 - m \frac{v_{10} + 5v_{20}}{48} \frac{x_1 + 3x_4}{x_6} \end{bmatrix} \tag{10}
 \end{aligned}$$

The original system is transformed into two third-order pseudo-linear systems under the action of the feedback control law. The coordinate transformation of the suspension module is shown in Figure 4.

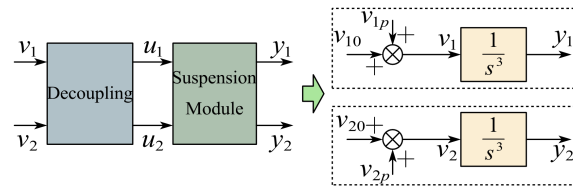


Figure 4. Coordinate transformation of the suspension module.

3.2. State Feedback Control

It can be seen from Figure 4 that the system has been decoupled into two independent subsystems. Therefore, controllers v_{10}, v_{20} can be designed. Firstly, neglecting the system uncertainty, controller v_{10} is designed as an example. The state space of the first third-order pseudo-linear system is represented as follows:

$$\begin{cases} \dot{z} = Az + Bv_{10} \\ y_1 = Cz \end{cases} \tag{11}$$

where

$$z = \begin{bmatrix} x_1 \\ x_2 \\ \dot{x}_2 \end{bmatrix}, A = \begin{bmatrix} 0 & 1 & 0 \\ 0 & 0 & 1 \\ 0 & 0 & 0 \end{bmatrix}, B = \begin{bmatrix} 0 \\ 0 \\ 1 \end{bmatrix}, C = \begin{bmatrix} 1 \\ 0 \\ 0 \end{bmatrix}^T$$

The system controllability matrix can be derived as follows:

$$M = [B \quad AB \quad A^2B] = \begin{bmatrix} 0 & 0 & 1 \\ 0 & 1 & 0 \\ 1 & 0 & 0 \end{bmatrix} \tag{12}$$

The rank of the controllability matrix of Equation (12) is as follows:

$$\text{rank}(M) = 3 \tag{13}$$

According to the rank criterion of system controllability, the system (11) is completely controllable. Therefore, the controller can be designed by the pole placement method.

Let the feedback control law be as follows:

$$v_{10} = -k_1(z_1 - d_{10}) - k_2z_2 - k_3z_3 = k_1d_{10} - K_1z \tag{14}$$

where $K_1 = [k_1 \quad k_2 \quad k_3]$ are the coefficients of the feedback control law; d_{10} is the expected gap value at point A.

According to the linear system theory, the characteristic polynomial of the closed-loop system is obtained by substituting (14) into (11).

$$\begin{aligned} T(s) &= \det[sI - (A - BK_1)] \\ &= s^3 + k_3s^2 + k_2s + k_1 \end{aligned} \tag{15}$$

The characteristic equation of (11) is described as follows:

$$s^3 + k_3s^2 + k_2s + k_1 = 0 \tag{16}$$

According to the actual requirements of the suspension system, the dynamic performance indicators of the system are set as follows:

- System overshoot: $\sigma \leq 5\%$;
- System peak time: $t_p \leq 0.1s$.

The formulas for overshoot and peak time are shown as follows:

$$\begin{cases} \sigma = e^{-\xi\pi/\sqrt{1-\xi^2}} \leq 5\% \\ t_p = \pi/(\omega_n\sqrt{1-\xi^2}) \leq 0.1s \end{cases} \quad (17)$$

The solution of Equation (17) is $\omega_n \geq 43.4$ rad/s and $\xi \geq 0.69$. Let $\xi = 0.707$, $\omega_n = 57$ rad/s, so the system's dominant poles can be taken as follows:

$$\begin{aligned} \lambda_{1,2} &= -\xi\omega_n \pm \omega_n\sqrt{\xi^2 - 1} \\ &= -40 \pm 40j \end{aligned} \quad (18)$$

In general, the distance between the non-dominant poles and the imaginary axis is 5 to 10 times that of the dominant poles. Therefore, the third pole can be set as $\lambda_3 = -400$.

According to the system poles, the characteristic equation can be obtained as follows:

$$s^3 + 480s^2 + 64,000s + 1,280,000 = 0 \quad (19)$$

Comparing Equations (16) and (19), the coefficients of the feedback control law are calculated as follows:

$$K_1 = [k_1 \quad k_2 \quad k_3] = [1,280,000 \quad 64,000 \quad 480] \quad (20)$$

The same pole configuration is performed for point B. The feedback linearization (FL) control law is as follows:

$$\begin{cases} v_{10} = -1,280,000(z_1 - d_{10}) - 64,000z_2 - 480z_3 \\ v_{20} = -1,280,000(z_4 - d_{20}) - 64,000z_5 - 480z_6 \end{cases} \quad (21)$$

where $[z_4 \quad z_5 \quad z_6] = [x_4 \quad x_5 \quad \dot{x}_5]$; d_{20} is the expected gap value at point B.

3.3. Linear Extended State Observer

Considering the system uncertainties, the state space of the first subsystem can also be written as follows:

$$\begin{cases} \dot{z}_1 = z_2 \\ \dot{z}_2 = z_3 \\ \dot{z}_3 = p(z, t) + v_0 \\ y = z_1 \end{cases} \quad (22)$$

where $p(z, t)$ represents the equivalent disturbance (v_{1p} or v_{2p}), and v_0 denotes the output of the controller (v_{10} or v_{20}).

Based on the concept of linear ESO, the original system Equation (22) can be extended as Equation (23) by expanding $p(z, t)$ into a new state variable z_4 .

$$\begin{cases} \dot{z}_1 = z_2 \\ \dot{z}_2 = z_3 \\ \dot{z}_3 = z_4 + v_0 \\ \dot{z}_4 = \dot{p}(t) \\ y = z_1 \end{cases} \quad (23)$$

The linear ESO can be designed as Equation (24):

$$\begin{cases} \dot{\hat{z}}_1 = \hat{z}_2 - \beta_1 e_1 \\ \dot{\hat{z}}_2 = \hat{z}_3 - \beta_2 e_1 \\ \dot{\hat{z}}_3 = \hat{z}_4 - \beta_3 e_1 + v_0 \\ \dot{\hat{z}}_4 = -\beta_4 e_1 \end{cases} \quad (24)$$

where $\hat{z} = [\hat{z}_1 \ \hat{z}_2 \ \hat{z}_3 \ \hat{z}_4]^T$ is the estimated state of $z = [z_1 \ z_2 \ z_3 \ z_4]^T$; $\beta_1, \beta_2, \beta_3,$ and β_4 are the gain of ESO; $e_1 = \hat{z}_1 - y$ is the observation error of z_1 .

We define estimation errors $e_2 = \hat{z}_2 - z_2, e_3 = \hat{z}_3 - z_3, e_4 = \hat{z}_4 - z_4$. The dynamics of the errors can be represented as follows:

$$\begin{cases} \dot{e}_1 = e_2 - \beta_1 e_1 \\ \dot{e}_2 = e_3 - \beta_2 e_1 \\ \dot{e}_3 = e_4 - \beta_3 e_1 \\ \dot{e}_4 = -\dot{p}(t) - \beta_4 e_1 \end{cases} \quad (25)$$

Equation (25) can be described as follows:

$$\dot{e} = \begin{bmatrix} -\beta_1 & 1 & 0 & 0 \\ -\beta_2 & 0 & 1 & 0 \\ -\beta_3 & 0 & 0 & 1 \\ -\beta_4 & 0 & 0 & 0 \end{bmatrix} e + \begin{bmatrix} 0 \\ 0 \\ 0 \\ -1 \end{bmatrix} \dot{p}(t) \quad (26)$$

where

$$e = \begin{bmatrix} e_1 \\ e_2 \\ e_3 \\ e_4 \end{bmatrix}, A_e = \begin{bmatrix} -\beta_1 & 1 & 0 & 0 \\ -\beta_2 & 0 & 1 & 0 \\ -\beta_3 & 0 & 0 & 1 \\ -\beta_4 & 0 & 0 & 0 \end{bmatrix}$$

According to the linear system theory, it is known that the system characteristic polynomial of Equation (23) is as follows:

$$\begin{aligned} T(s) &= \det[sI - A_e] \\ &= s^4 + \beta_1 s^3 + \beta_2 s^2 + \beta_3 s + \beta_4 \end{aligned} \quad (27)$$

The characteristic equation is described as follows:

$$s^4 + \beta_1 s^3 + \beta_2 s^2 + \beta_3 s + \beta_4 = 0 \quad (28)$$

In order to facilitate parameter tuning, the polynomial of ESO can be given as $(s + \omega_c)^4$. ω_c denotes the bandwidth of ESO, which is the only parameter that needs to be tuned. Comparing Equation (28) and $(s + \omega_c)^4 = 0$, the gain of ESO can be designed as follows:

$$\begin{cases} \beta_1 = 4\omega_c \\ \beta_2 = 6\omega_c^2 \\ \beta_3 = 4\omega_c^3 \\ \beta_4 = \omega_c^4 \end{cases} \quad (29)$$

Compensation is performed in the controller based on the observed disturbances. The feedback linearization with ESO (FLESO) control law is as follows:

$$\begin{cases} v_{10} = -1,280,000(z_1 - d_{10}) - 64,000z_2 - 480z_3 - \hat{p}_1 \\ v_{20} = -1,280,000(z_4 - d_{20}) - 64,000z_5 - 480z_6 - \hat{p}_2 \end{cases} \quad (30)$$

The block diagram of FLESO control for the suspension module system is shown in Figure 5.

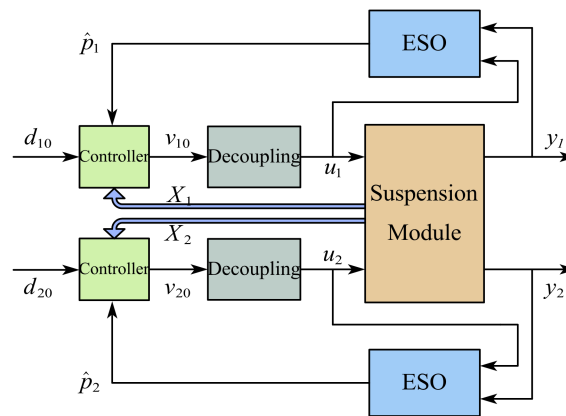


Figure 5. The block diagram of FLESO control.

4. Simulation and Experimental Results

The effectiveness of the designed FLESO control strategy is evaluated through comparative simulation and experimental comparisons with the conventional PID controller on the full-size bogie experimental platform, as shown in Figure 6. The simulation and experimental parameters [21] of the suspension module control system are shown in Table 1. The controller parameters are shown in Table 2.

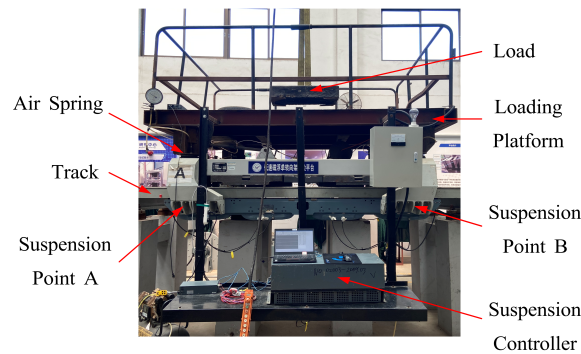


Figure 6. The full-size bogie experimental platform.

Table 1. Parameters of the suspension module control system.

Symbol	Description	Value	Unit
m	Mass of a suspension module	900	kg
F_{N1}, F_{N2}	Forces from air springs	12,000	N
A	The effective area of each magnet pole	0.0186	m ²
l	Length of an electromagnet	0.65	m
μ_0	Permeability of vacuum	$4\pi \times 10^{-7}$	H/m
R	Coil resistance of a set of electromagnets	1	Ω
g	Acceleration of gravity	9.8	m/s ²
δ_0	Nominal air gap at the operation point	8	mm
N	Number of coil turns of each electromagnet	320	–

Table 2. Parameters of PID controller and ESO.

Symbol	Description	Value	Unit
k_p	The proportional parameter of PID controller	4500	–
k_i	The integral parameter of PID controller	4	–
k_d	The differential parameter of PID controller	950	–
ω_c	The bandwidth of ESO	5000	–

4.1. Numerical Simulations

The suspension module is initially suspended at 8 mm. Subsequently, the following three disturbances are applied to the system under different controllers.

Case 1: Trajectory tracking;

Case 2: Suspension with periodic perturbation;

Case 3: Suspension with load disturbance.

The simulation parameters are shown in Tables 1 and 2.

4.1.1. Case 1: Trajectory Tracking

Point A is subjected to a 1 mm square wave disturbance lasting 1 s. The simulation results of the PID controller and the FLESO controller are shown in Figures 7 and 8.

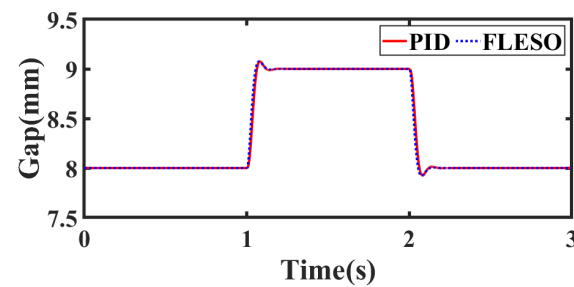


Figure 7. Simulation results: gap response of point A.

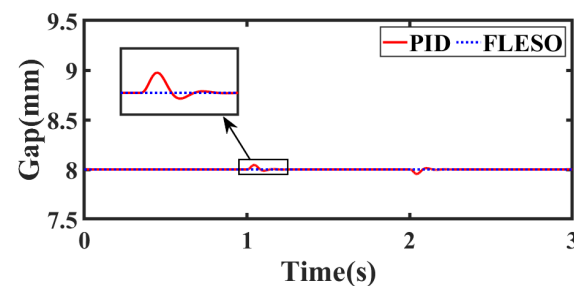


Figure 8. Simulation results: gap response of point B.

From the above simulation results in Figures 7 and 8, it can be learned that when using the PID controller, the changes in the gap at point A affect the gap at point B. However, the FLESO controller effectively maintains the stability of point B when point A experiences gap fluctuations under the same conditions. It shows the satisfying decoupling performance achieved by the designed FLESO controller.

4.1.2. Case 2: Suspension with Periodic Perturbation

Assume that the system is disturbed by the following periodic perturbations consisting of model error and external disturbances:

$$\begin{cases} f_{p1}(t) = f_{p2}(t) = 5(\sin 80\pi t + 2 \cos 70\pi t) \\ u_{p1}(t) = u_{p2}(t) = 60 \cos(100\pi t) \end{cases} \quad (31)$$

The system is transformed into two identical pseudo-linear systems after decoupling, as can be seen in Figure 4, since only the curves of point A are presented. Figure 9 shows the observed performance of ESO for equivalent disturbances. According to Equation (9), the equivalent disturbance at point A can be obtained as follows:

$$\begin{cases} v_{p1} = L_p L_f^2 h(x) + d(L_p L_f h(x)) / dt \\ = -\frac{80Kx_3}{m(3x_1 + x_4)^2} u_{p1}(t) + \frac{16Kx_6}{m(x_1 + 3x_4)^2} u_{p2}(t) + \dot{f}_{p1}(t) \end{cases} \quad (32)$$

It can be observed from Figure 9 that the ESO takes approximately 0.05 s to converge, and the estimation error remains below 5% of the actual value.

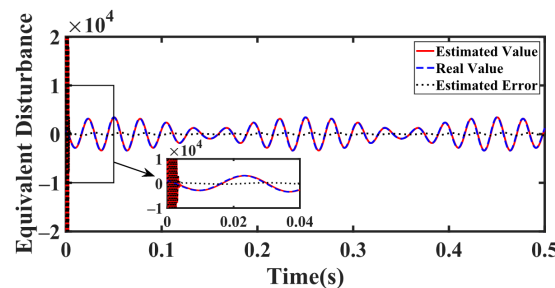


Figure 9. Estimated performance of the ESO.

The response performance of three kinds of controllers (PID, FL, and FLESO) under periodic disturbances is shown in Figure 10. The perturbation compensation of FLSEO is added to the system at 0.01 s to keep the system stable. From Figure 10, it can be seen that the PID controller is weak, and the disturbance’s influence on system stability is very high. However, the FL controller effectively reduces the influence of the disturbance on the system. Furthermore, with the implementation of the FLESO controller, the suspension system achieves even greater stability. The fluctuation amplitude of the FLESO controller is reduced to approximately 5% of that observed with the PID controller.

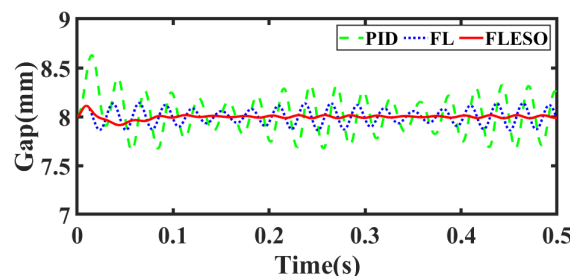


Figure 10. Response curves of the suspension system under periodic perturbations.

4.1.3. Case 3: Suspension with Load Disturbance

At the time of 0.1 s, a downward force of 2400 N is applied to the suspension system. Figure 11 illustrates the control performance of the PID, FL, and FLESO controllers under load disturbance.

As shown in Figure 11, the PID controller exhibits a maximum deviation of nearly 0.5 mm from the operation point. The FL controller effectively suppresses the disturbances, reducing the fluctuation amplitude by approximately 88% compared to the PID controller. Furthermore, the FLESO controller further reduces the fluctuation amplitude to within 1% of the PID controller. This demonstrates that the FLESO controller possesses a stronger ability to resist disturbances compared to the PID and FL controllers.

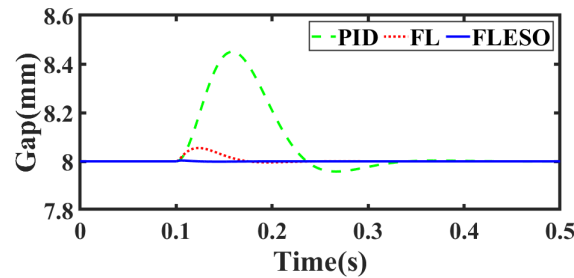


Figure 11. Response curves of the suspension system under load disturbance.

4.2. Experimental Results

In order to further verify the performance of the FLESO controller in real systems, three sets of experiments are conducted on the experimental platform shown in Figure 6:

- Scenario 1: Trajectory tracking;
- Scenario 2: Suspension with load disturbance;
- Scenario 3: Suspension with track step disturbance.

4.2.1. Scenario 1: Trajectory Tracking

Experiment scheme: After the ESO converges, disturbance compensation is introduced to the system which is suspended at 8 mm. Subsequently, a ± 2 mm square wave disturbance with a period of 3 s is applied at point A. The same experiments were conducted using the conventional PID controller as well as the proposed FLESO controller. The response curves of the suspension gap are shown in Figures 12 and 13.

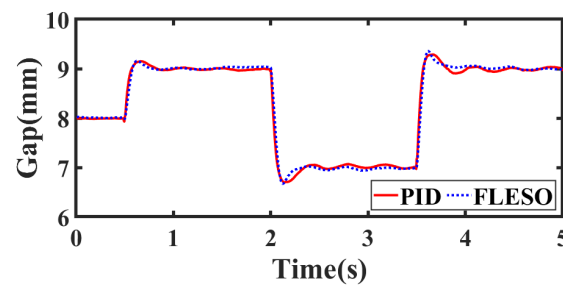


Figure 12. Experimental results: gap response of point A.

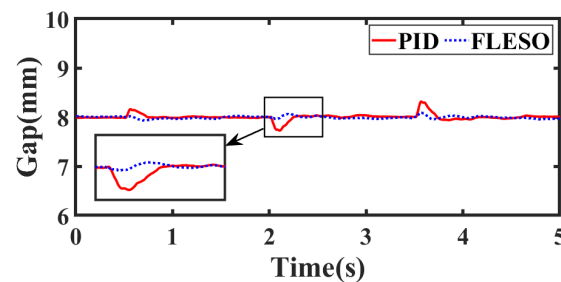


Figure 13. Experimental results: gap response of point B.

As shown in Figures 12 and 13, the conventional PID controller fails to suppress the fluctuation of point B when point A is disturbed. The maximum gap fluctuation of point

B reaches approximately 0.3 mm. In contrast, the proposed FLESO controller effectively controls the gap fluctuation at point B within 0.1 mm. The results show that the FLESO controller has satisfying decoupling performance.

4.2.2. Scenario 2: Suspension with Load Disturbance

Experiment scheme: A 240 kg load is applied to the loading platform, as shown in Figure 6, when the system is suspended steadily. The load is subsequently removed after the system stabilizes again. The gap response curves of the PID controller and FLESO controller are shown in Figures 14 and 15.

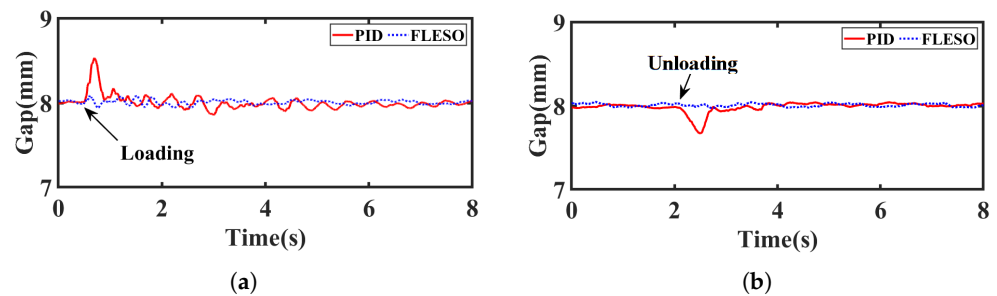


Figure 14. Experimental results: gap response of point A. (a) Loading; (b) unloading.

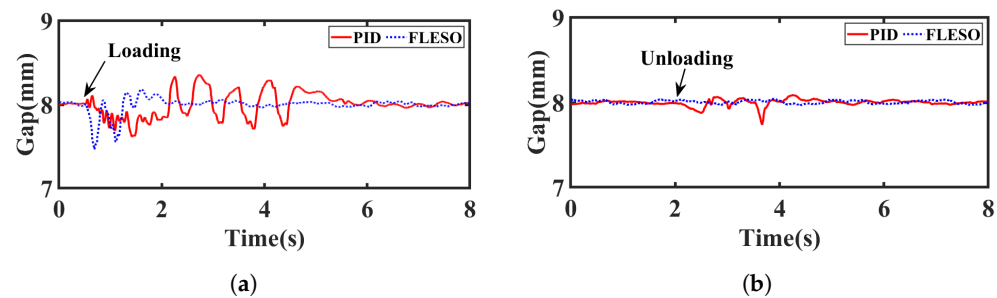


Figure 15. Experimental results: gap response of point B. (a) Loading; (b) unloading.

As observed in Figures 14 and 15, when a load disturbance is introduced, the system controlled by the PID controller exhibited significant fluctuations. The amplitude of fluctuations at point A and point B reach 0.533 mm and 0.386 mm, respectively. Moreover, the system required approximately 8 s to recover stability. However, the system controlled by the FLESO controller demonstrated stronger robustness against the same disturbance. The amplitude of fluctuations of point A is reduced to 0.084 mm. Furthermore, the system only requires about 3 s to regain stability again. When the load is removed, the system using the PID controller experiences some fluctuations due to perturbations. In contrast, the system controlled by the FLESO controller remains stable near the operating point, with the suspension gap being hardly affected. This demonstrates that the proposed FLESO control strategy can effectively handle the load uncertainties in the system.

4.2.3. Scenario 3: Suspension with Track Step Disturbance

The tracks of the maglev train are interconnected by joints, as shown in Figure 16. And the schematic diagram of the track joint is shown in Figure 17. The gap width of the joint is 23 mm, and the difference of the joint step is 4 mm.

In order to verify the performance of the FLESO controller when the suspension system passes through the joints, the following experiments are conducted. First the experimental platform is suspended around 8 mm. Then, the experimental platform is pushed and moved at a certain speed. The suspension module decelerates until it comes to a stop after point A passes completely through the track joint. Two identical sets of experiments were performed using the PID controller and FLESO controller. The experimental results are shown in Figures 18 and 19.



Figure 16. The position of the track joint.

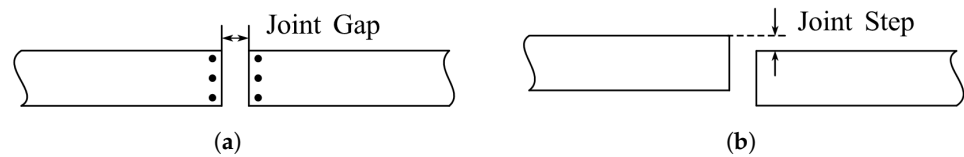


Figure 17. The diagram of the track joint. (a) Vertical view; (b) side view.

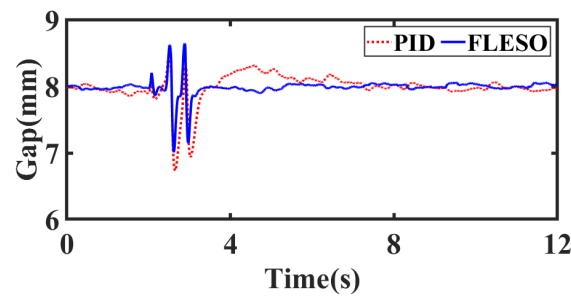


Figure 18. Experimental results: gap response of point A.

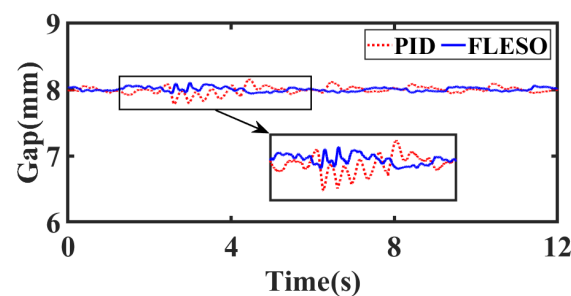


Figure 19. Experimental results: gap response of point B.

Based on the results shown in Figures 18 and 19, the gap sensor of point A starts to pass the joint at about 2.7 s and completes the passage one second later. The suspension system takes about 4 s to converge to the expected suspension gap under the PID controller. And the range of fluctuation of the gap at point B is $[-0.233 \text{ mm}, 0.152 \text{ mm}]$. It takes approximately 5 s for the suspension system to regain stability. When using the FLESO controller, the fluctuation range of the gap at point B is reduced to $[-0.038 \text{ mm}, 0.102 \text{ mm}]$. Moreover, the suspension system regains stability in just 1.5 s. Therefore, the proposed FLESO controller can effectively suppress the influence caused by the track steps on the maglev system.

5. Conclusions

In this paper, a decoupling control strategy based on feedback linearization and ESO is designed to suppress the effect of inner coupling, load variations, and parameter perturbations in a magnetic suspension module. The uncertainties present in the system are estimated by ESO and compensated in the state feedback controller to improve the system's robustness.

The performance of this proposed strategy is tested for several experiments, including trajectory tracking, load disturbances, and track step disturbances. The results illustrate that the proposed method can reduce the effect of coupling between suspension points by 72.6% compared to the traditional PID controller. In addition, when the load changes, the method can not only effectively suppress the gap fluctuation of the system, but also reduce the adjustment time to approximately 37% of the traditional PID controller. The decoupling control strategy presented in this paper effectively improves the stability of the magnetic suspension system.

Author Contributions: Conceptualization, Q.L. and P.L.; methodology, Q.L.; software, Q.L.; validation, Q.L. and D.Z.; formal analysis, J.L.; investigation, Q.L. and P.L.; resources, J.L.; data curation, J.L. and M.Q.; writing—original draft preparation, Q.L.; visualization, P.Y. and M.Q.; supervision, J.L.; project administration, J.L. All authors have read and agreed to the published version of the manuscript.

Funding: This work was supported by the National Key Research and Development Program of China (grant number 2016YFB1200601).

Data Availability Statement: Not applicable.

Conflicts of Interest: The authors declare no conflict of interest.

References

1. Lee, H.W.; Kim, K.C.; Lee, J. Review of maglev train technologies. *IEEE Trans. Magn.* **2006**, *42*, 1917–1925. [\[CrossRef\]](#)
2. Gou, J. Development status and global competition trends analysis of maglev transportation technology based on patent data. *Urban Rail Transit* **2018**, *4*, 117–129. [\[CrossRef\]](#)
3. Cassat, A.; Jufer, M. Maglev projects technology aspects and choices. *IEEE Trans. Appl. Supercon.* **2002**, *12*, 915–925. [\[CrossRef\]](#)
4. Nakamura, S. Development of high speed surface transport system (HSST). *IEEE Trans. Magn.* **1979**, *15*, 1428–1433. [\[CrossRef\]](#)
5. Park, D.Y.; Shin, B.C.; Han, H. Korea's urban maglev program. *Proc. IEEE* **2009**, *97*, 1886–1891. [\[CrossRef\]](#)
6. Yan, L. Progress of the maglev transportation in china. *IEEE Trans. Appl. Supercon.* **2006**, *16*, 1138–1141. [\[CrossRef\]](#)
7. Dai, G.; Liu, G.; Liu, W.; Chen, Y.; Yang, L. Design and construction of concrete simply-supported guideway beam in the changsha maglev line, china. *Struct. Eng. Int.* **2017**, *27*, 569–574. [\[CrossRef\]](#)
8. Xu, Y.; Zhao, Z.; Long, Z.; Wen, T. Performance optimization of maglev train's electromagnetic levitation system: Control structure and algorithm. *IEEE Trans. Autom. Sci. Eng.* **2023**, 1–11. [\[CrossRef\]](#)
9. Zeng, J.; Xia, W.; Xiang, X.; Long, Z. Research on the mechanism and control characteristics of vehicle-track beam coupling vibration for medium-speed maglev vehicle. *IEEE Trans. Transp. Electr.* **2022**, *8*, 3236–3246. [\[CrossRef\]](#)
10. Yang, Q.; Chi, Z.; Wang, L. Uncertainty analysis of suspension system caused by horizontal misalignment and its suppression method. *Machines* **2022**, *10*, 977–999. [\[CrossRef\]](#)
11. Li, Y.; Yu, P.; Zhou, D.; Li, J. Magnetic flux feedback strategy to suppress the gap fluctuation of low speed maglev train caused by track steps. In Proceedings of the 37th Chinese Control Conference (CCC 2018), Wuhan, China, 25–27 July 2018; pp. 983–989. [\[CrossRef\]](#)
12. Nguyen, D.; Nguyen, T. Evaluate the stability of the vehicle when using the active suspension system with a hydraulic actuator controlled by the OSMC algorithm. *Sci. Rep.* **2022**, *12*, 19364. [\[CrossRef\]](#)
13. Li, H.; Ke, Z.; Huang, H.; Li, Y.; Wang, S.; Deng, Z. Vibration suppression of high-temperature superconducting maglev system via semi-active suspension system. *Phys. C Supercond.* **2022**, *601*, 1354109–1354117. [\[CrossRef\]](#)
14. Yu, P.; Li, J.; Wang, L. Research on the influence of track periodic short-wave irregularity on low-speed maglev train. In Proceedings of the 35th Chinese Control Conference (CCC 2016), Chengdu, China, 27–29 July 2016; pp. 9305–9310. [\[CrossRef\]](#)
15. Munro, N. Applications of the inverse nyquist array design method. In Proceedings of the IEEE Conference on Decision and Control Including the 15th Symposium on Adaptive Processes, Clearwater, FL, USA, 1–3 December 1976; pp. 348–353. [\[CrossRef\]](#)
16. Descusse, J.; Moog, C.H. Dynamic decoupling for right-invertible nonlinear systems. *Syst. Control. Lett.* **1987**, *8*, 345–349. [\[CrossRef\]](#)
17. Lokesh, N.; Mishra, M.K. Design of a decoupled sliding mode control for four-leg distribution static compensator. *IEEE Trans. Power Deliv.* **2022**, *37*, 5014–5024. [\[CrossRef\]](#)

18. Ding, J.; Wu, M.; Xiao, M. Nonlinear decoupling control with $pi^\lambda d^\mu$ neural network for mimo systems. *IEEE Trans. Neural Netw. Learn. Syst.* **2022**, 1–8. [[CrossRef](#)]
19. Liu, D.; Li, J.; Zhang, K. Design of Nonlinear Decoupling Controller for Double-electromagnet Suspension System. *Acta Anat. Sin.* **2006**, *32*, 321–328.
20. Leng, P.; Li, Y.; Zhou, D.; Li, J.; Zhou, S. Decoupling control of maglev train based on feedback linearization. *IEEE Access* **2019**, *7*, 130352–130362. [[CrossRef](#)]
21. He, G.; Li, J.; Cui, P. Nonlinear control scheme for the levitation module of maglev train. *J. Dyn. Syst. Meas. Control Trans. ASME* **2016**, *138*, 1–8. [[CrossRef](#)]
22. Sun, Y.; Yang, L.; Xu, J.; Wang, S. Decoupling levitation control of maglev train based on backstepping control. In Proceedings of the 2021 International Conference on Sensing, Measurement & Data Analytics in the Era of Artificial Intelligence (ICSMD 2021), Nanjing, China, 21–23 October 2021; pp. 1–6. [[CrossRef](#)]
23. Xu, J.; Chen, C.; Sun, Y. Nonlinear dynamic characteristic modeling and adaptive control of low speed maglev train. *Int. J. Appl. Electromagn. Mech.* **2020**, *62*, 73–92. [[CrossRef](#)]
24. Chen, C.; Xu, J.; Lin, G.; Sun, Y.; Gao, D. Fuzzy adaptive control particle swarm optimization based on t-s fuzzy model of maglev vehicle suspension system. *J. Mech. Sci. Technol.* **2020**, *34*, 43–54. [[CrossRef](#)]
25. Sun, Y.; Xu, J.; Xu, H.; Cai, W.; Lin, G. Backstepping Sliding Mode Control for Magnetic Suspension System of Maglev Train with Parameter Perturbations and External Disturbance. In Proceedings of the Advances in Applied Nonlinear Dynamics, Vibration and Control (ICANDVC 2021), Hong Kong, China, 23–25 August 2021; pp. 253–267. [[CrossRef](#)]
26. Ni, F.; Mu, S.; Kang, J.; Xu, J. Robust controller design for maglev suspension systems based on improved suspension force model. *IEEE Trans. Transp. Electrification* **2021**, *7*, 1765–1779. [[CrossRef](#)]
27. Leng, P.; Yu, P.; Gao, M.; Li, J.; Li, Y. Optimal Control Scheme of Maglev Train Based on The Disturbance Observer. In Proceedings of the Chinese Control Conference (CCC 2019), Guangzhou, China, 27–30 July 2019; pp. 1935–1940. [[CrossRef](#)]
28. Verma, A.; Patel, V.; Guha, D. Disturbance Observer-based Resilient Controller for Nonlinear Maglev System. In Proceedings of the IEEE 9th Uttar Pradesh Section International Conference on Electrical, Electronics and Computer Engineering (UPCON 2022), Prayagraj, India, 2–4 December 2022; pp. 1–6. [[CrossRef](#)]
29. Sun, Y.; Xie, S.; Xu, J.; Lin, G. A Robust Levitation Control of Maglev Vehicles Subject to Time Delay and Disturbances: Design and Hardware Experimentation. *Appl. Sci.* **2020**, *10*, 1179–1196. [[CrossRef](#)]
30. Sun, Y.; Xu, J.; Wu, H.; Lin, G.; Mumtaz, S. Deep learning based semi-supervised control for vertical security of maglev vehicle with guaranteed bounded airgap. *IEEE trans. Intell. Transp. Syst.* **2021**, *22*, 4431–4442. . [[CrossRef](#)]
31. Chen, C.; Xu, J.; Ji, W.; Rong, L.; Lin, G. Sliding Mode Robust Adaptive Control of Maglev Vehicle's Nonlinear Suspension System Based on Flexible Track: Design and Experiment. *IEEE Access* **2019**, *7*, 41874–41884. . [[CrossRef](#)]
32. Sun, Y.; Xu, J.; Lin, G. Adaptive neural network control for maglev vehicle systems with time-varying mass and external disturbance. *Neural. Comput. Appl.* **2023**, *35*, 12361–12372. [[CrossRef](#)]
33. Wang, Z.; Long, Z.; Li, X. Track Irregularity Disturbance Rejection for Maglev Train Based on Online Optimization of PnP Control Architecture. *IEEE Access* **2019**, *7*, 12610–12619. [[CrossRef](#)]
34. Sahoo, A.K.; Mishra, S.K.; Acharya, D.S.; Sahu, S.S.; bibinfoauthorPaul, S.; bibinfoauthorGupta, V.K. Identification and control of Maglev system using fractional and integer order PID controller. *J. Intell. Fuzzy Syst.* **2023**, *44*, 7277–7289. [[CrossRef](#)]
35. Teklu, E.A.; Abdissa, C.M. Genetic Algorithm Tuned Super Twisting Sliding Mode Controller for Suspension of Maglev Train with Flexible Track. *IEEE Access* **2023**, *11*, 30955–30969. [[CrossRef](#)]

Disclaimer/Publisher's Note: The statements, opinions and data contained in all publications are solely those of the individual author(s) and contributor(s) and not of MDPI and/or the editor(s). MDPI and/or the editor(s) disclaim responsibility for any injury to people or property resulting from any ideas, methods, instructions or products referred to in the content.